Discover Applied Sciences

RESEARCH Open Access

Multidisciplinary design optimization of a transverse flux machine based on a multi-step loss calculation method

Tim Jonathan Lefringhausen[1], Simon Knecht[1*], Nejila Parspour[2] and Albert Albers[1]

*Correspondence:
Simon Knecht
simon.knecht@kit.edu
[1]Institute of Product Engineering, Karlsruhe Institute of Technology, Kaiserstr. 12, 76131 Karlsruhe, Baden-Württemberg, Germany
[2]Institute of Electrical Energy Conversion, University of Stuttgart, Pfaffenwaldring 47, 70569 Stuttgart, Baden-Württemberg, Germany

Abstract
A transverse flux machines is a special type of electrical machine that offers advantages in terms of torque and power density. Due to the complex simulation, design and manufacturing, transverse flux machines are rarely used despite their many possible applications. The three-dimensional magnetic flux guidance results in a complex geometry of the stator core. As the conventional design of axially stacked electrical steel sheets is not feasible for this type of motor, new manufacturing methods are being researched. In addition, few procedures for simulation and design have been available to date. This paper presents an approach that enables the optimization of an additively manufactured stator core with respect to both efficiency and thermal behavior. In order to efficiently simulate the various power losses of the motor, the results of a 3D-FEM simulation as well as empirical models were combined in several steps. As there is a strong interaction between the thermal and electromagnetic domain for this type of motor, both were simulated iteratively coupled. The shape of the stator core was optimized for low and high speeds, taking into account the respective heating, which led to an improvement in efficiency of more than 5 %pt. in both cases.

Keywords Transverse flux machine, Multidisciplinary simulation, Parametric optimization, Finite element analysis

1 Introduction

The probably greatest challenge of our time is climate change, the combat of which requires significant changes in industry, mobility, and transportation. Electric drives already represent the most sustainable and efficient solution in most applications today, forming the basis for e.g. future mobility. Typically, radial flux or axial flux motors are combined with gearboxes to meet the required torque demands. However, this approach comes with various disadvantages: increased weight, size, losses, and noise emissions. Costs, maintenance efforts, and gearbox wear are also undesirable.

Transverse flux machines (TFM) are a variant of electric machines that can achieve a very high torque density while maintaining high efficiency. Thanks to these

characteristics, direct drives are conceivable for many applications. Research is being conducted, for example, on their use as traction motors in cars, buses, trams, or as hub motors in e-bikes. Their application in industrial robots, ships, or aviation is also being explored. Although TFMs theoretically offer many advantages, they have not yet become prevalent. Reasons for this include the complex manufacturing process and the demanding modeling and simulation. As part of the research cluster *InnovationCampus – Mobility of the Future*, funded by the state of Baden-Württemberg, Germany, research is being conducted on both innovative manufacturing processes and future mobility solutions. This paper shows a multi-step and multidisciplinary simulation model to optimize both the electromagnetic and thermal behavior of a TFM. By using an iteratively coupled approach, the geometry of the motor's stator can be optimized for different combinations of operating states and thermal conditions.

1.1 Transverse flux machine

Rotating electrical machines can be classified by the geometric orientation between the plane of the magnetic flux to their axis of rotation. The most common type of electric motor uses magnetic flux oriented radially to the axis of rotation. This type of motor is called radial flux machine, or RFM (Fig. 1a). The conductor windings are usually wound around slots in the stator and their effective part is oriented parallel to the axis of rotation [1]. In an axial flux machine (AFM), the individual stator windings are arranged around magnetic cores in a plane perpendicular to the axis of rotation. The rotor and stator lie next to each other along the axis, as shown in Fig. 1b. The air gap therefore lies in a plane perpendicular to the direction of rotation and the field lines in the air gap are aligned axially.

In a TFM there is only one winding per phase, which is arranged in a ring and coaxially around the axis of rotation. The design difference between the TFM and the other two arrangements lies in the spatially separate guidance of the magnetic flux and the electric current [1]. The magnetic circuit is transverse to the axis of rotation as shown in Fig. 1c. Rotating TFMs can be further subdivided into subcategories. For example, synchronous machines with permanent magnets or electrical excitations as well as asynchronous machine are possible using this design [2].

While in radial and axial flux machines the size of the windings and stator teeth compete for the available installation space, separate dimensioning and optimization is

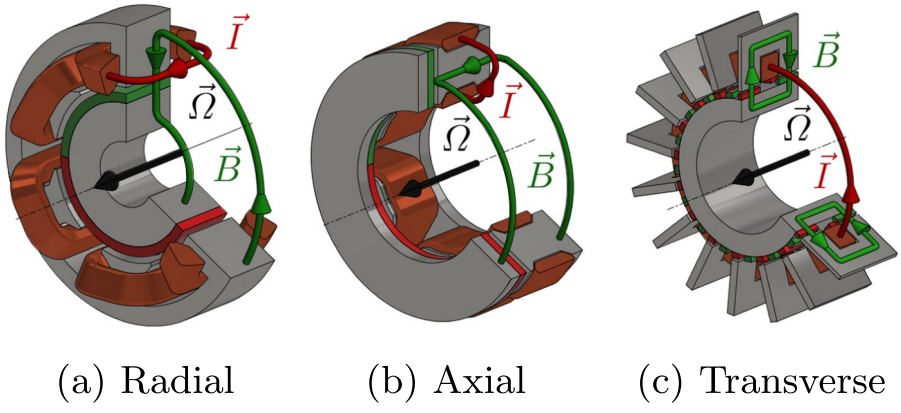

Fig. 1 Different machine types distinguished by the different orientation of the magnetic flux plane (adapted from [2])

possible with TFMs. This enables a much finer pole pitch, which increases the torque density [3]. Another advantage is the elimination of winding heads and thus some of the ohmic copper losses [4]. This allows TFMs to be realized that have a higher gravimetric power and torque density, a higher volumetric torque density and lower torque-related losses and mass inertia than conventional motor designs [5]. The high torque density of TFM has already been demonstrated in previous research results [2, 6, 7].

This means that the TFM has the potential to provide the required torque in certain applications with no or less gear reduction, as demonstrated by [8] for the design of a TFM for electrical vehicles. The TFM is particularly attractive as a traction motor for electric vehicles due to its ability to deliver very high torque at low rotational speeds, enabling direct-drive architectures without the need for multi-stage gearboxes. In such a drivetrain, the TFM's high torque density can provide strong acceleration performance while reducing mechanical complexity, noise, and maintenance of the gearbox. Its compact form factor also offers greater flexibility for integration near or within the wheel area, making in-wheel or near-wheel motor concepts feasible. Another promising application scenario for TFMs is their use in industrial robotics and automation systems [6]. Robots often require compact actuators capable of delivering high torque with precise, dynamic control, especially in joints that must support significant loads while maintaining fine positioning accuracy. The TFM's high torque density and the absence of large winding heads make it well suited for integration into joint actuators where space is limited. Further advantages are a higher accuracy of the electromechanical actuators and better noise behavior [2]. These properties make the use of TFM attractive for a variety of applications. Research is being carried out into its use as a traction motor for electric cars [9], trams [10], electric bicycles [11], and as part of a hybrid drivetrain for buses [12]. Other potential applications include marine propulsion systems [13], aerospace applications [14], electric tools [15] and as a generator in wind turbines [16].

Although the principle of the TFM was already described in 1890 by [17] and the aforementioned advantages, it has not yet become established on a large scale [6]. One reason for this is a high cogging torque and a high torque ripple caused by strong fluctuations in the reluctance force [2]. These fluctuations lead to vibrations and noise during operation [3]. For electric vehicles, this may translate into reduced driving comfort or the need for more sophisticated control algorithms and mechanical damping solutions, all of which increase system cost and complexity. In industrial robotics or machine tools, torque ripple can impair positioning accuracy and dynamic response, counteracting one of the key advantages that TFMs can offer. Another problem is the comparatively high power factor of TFM [18]. As a quotient of the active power and apparent power, this should be as close to one as possible to avoid overdimensioning and additional losses in the power electronics [2]. The design of the stator also poses a significant challenge. Soft magnetic materials with low electrical conductivity are required in order to achieve a high magnetic flux density with low eddy current losses due to induction. However, they typically have lower magnetic permeability and may introduce higher losses compared to conventional electrical steels. Due to the three-dimensional magnetic flux and often complex geometries, a conventional design consisting of axially stacked layers of electrical steel is not optimal. Various possibilities are being researched to solve this problem. The most common approach is the use of soft magnetic composite materials (SMC) [19]. Constructions made from differently orientated stacks of electrical steel [20]

or deformed electrical steel [21] are also being investigated but come with a drastically increased manufacturing effort.

In combination, these drawbacks mean that while TFMs offer exceptional theoretical torque density, their practical implementation requires overcoming significant design, manufacturing and operational challenges. As a result, TFMs are currently most viable in niche applications where high torque at low speed is essential, and where system-level benefits outweigh the increased development and production effort. Continued research in materials, simulation-driven optimization, and advanced manufacturing is therefore essential to reduce these barriers and enable broader industrial deployment.

This paper focuses on a comparatively new stator manufacturing method, that is, additive manufacturing from iron or iron alloys. The manufacturing process of powder bed-based fusion using a laser beam (L-PBF) offers a wide range of design and optimization options [22]. One of the biggest challenges of such stator cores is their high electrical conductivity and thus the eddy current losses during operation. This problem can be addressed with various approaches. Production using L-PBF makes it possible to use iron alloys with lower electrical conductivity, which cannot be processed using other production methods. In addition, research is being conducted by [23] into ways of adding layers of another material with lower conductivity during additive manufacturing to imitate the function of electrical steel sheets. The motor simulated in this work has thin slots in the stator, which are introduced during additive manufacturing and reduce eddy current losses by increasing the electrical resistance mainly in the circumferential direction [22, 24]. The slots' influence on the structural integrity was already investigated by [25]. In this work, we focus on the electromagnetic-thermal coupling and design optimization.

Different types of losses occur in electrical machines. In addition to ohmic losses in the windings (P_{Cu}) and mechanical losses such as friction and air drag (P_{mech}), the so-called iron losses (P_{Fe}) are particularly significant for the simulation. Iron losses are a combination of three loss components that occur during the remagnetization of iron cores, namely eddy current, hysteresis, and excess losses (P_{ec}, P_{hy} and P_{ex}, respectively).

These losses are usually calculated using models that can be divided into three groups. The first group of models is the mathematical hysteresis models, such as the Preisach model or the Jiles-Artherton model. These models determine the hysteresis losses by integrating the area formed by the hysteresis loop of the material with changing magnetization [26].

The second group of models is the Steinmetz equation, first published by [27], and its variants (xSE) [26].

$$P_{Fe} = C_{hy} \cdot \hat{B}^{\alpha} \cdot f + C_{ec} \cdot \hat{B}^2 \cdot f^2 \tag{1}$$

In the Steinmetz equation, the iron losses are calculated using coefficients C_{hy} and C_{ec} for hysteresis losses and eddy current losses, respectively, which have to be measured for the material. The Steinmetz equation without any modifications is only applicable at ideal sinusoidal changing flux densities. For different forms of excitement, modified and improved versions of the Steinmetz equation must be used. Examples are the generalized Steinmetz equation (GSE), modified Steinmetz equation (MSE) or the natural Steinmetz equation (NSE) [26].

The third, and most commonly used group of models for the calculation of iron losses are the models of loss separation, like the Bertotti model, first published by [28].

$$P_{Fe} = C_{hy} \cdot \hat{B}^2 \cdot f + C_{ec} \cdot \hat{B}^2 \cdot f^2 + C_{ex} \cdot \hat{B}^{1.5} \cdot f^{1.5} \tag{2}$$

In addition to the eddy current losses and hysteresis losses, these models take into account a further component, the excess losses with the coefficient C_{ex}.

The above models for calculating iron losses are based on one-dimensional, alternating magnetization. Especially when using SMC, consideration of three-dimensional, rotating magnetization in the modeling of iron losses is crucial [29, 30].

The aforementioned three-dimensional magnetic flux increases the complexity of TFM simulation models. Since a simplification by two-dimensional or symmetric simulation models, as is possible for AFM and RFM, is usually not possible for a TFM, a three-dimensional simulation model must be used which greatly increases the computational effort [2]. This is especially true for simulation-based iterative optimization methods, where a simulation is solved in each iteration. The challenge of high computational cost for a 3D-FEM can be managed with by combining 3D-FEM with surrogate-based optimization [31–33]. [34] conducted a multi-objective optimization of a TFM, combining 3D-FEM with genetic algorithms to tackle the complex optimization problem. Another multi-objective optimization method for a TFM was proposed by [35], where the torque ripple was included in the objective function and manufacturing uncertainties were considered. Furthermore, 3D-FEM was coupled with system-level design optimization to generate overall optimized designs.

The complexity increases further when considering multidisciplinary simulation and optimization, such as when considering and coupling the electromagnetic and thermal domains. Often times, the electromagnetic domain defines the stator design, while other domains such as thermal and mechanical are evaluated only afterwards [36–39]. Ref. [40] showed with thermal simulations of a TFM, that the temperature rise during operation is substantial and non-uniform throughout the stator. This necessitates a detailed treatment of both the electromagnetic and the thermal domain for design optimization of a TFM. Numerous publications exist on the multidisciplinary optimization of electric motors, taking thermal effects into account, such as [41–43]. However, little work was done on multidisciplinary optimization of a TFM. A multidisciplinary electromagnetic-thermal optimization of a TFM was presented by [44], however only little information was given on the optimization procedure. Furthermore, the involved domains were coupled only one-way and therefore did not interact with each other. Ref. [45] gives an overview of interactions between the electromagnetic, thermal and mechanical domain in electric machines. In the context of industrial applications, the majority of these interactions can be disregarded, as their impact on machine efficiency is considered negligible. However, especially the dependency of material properties on temperature must be accounted for in an accurate multidisciplinary design optimization.

2 Simulation model

The simulation model of the TFM was created using the commercial FEM simulation software COMSOL Multiphysics 6.1 and is based on the simulation models from [24] and [22]. The geometry of the stator core of the TFM is based on the prototype designed by [6]. This TFM was designed for use in a shoulder joint motor for robotic applications

Table 1 Operating parameters of the baseline TFM [22]

Parameter	Symbol	Value
Nominal speed	n_{nom}	$1100\,\mathrm{min}^{-1}$
Torque	T	$0.8\,\mathrm{Nm}$
Mechanical power	P_{out}	$105.5\,\mathrm{W}$

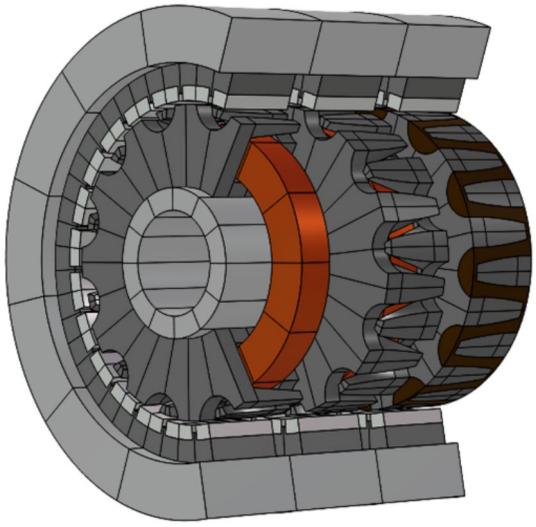

Fig. 2 Overview of motor design

Table 2 Geometric dimensions of the baseline TFM based on the design by [6]

Parameter	Symbol	Value
Outer motor radius	r_a	$34\,\mathrm{mm}$
Motor axial length	l_m	$49.8\,\mathrm{mm}$
Phase axial length	l_{Ph}	$11.6\,\mathrm{mm}$
Outer stator radius	$r_{St,o}$	$21\,\mathrm{mm}$
Inner stator radius	$r_{St,i}$	$10\,\mathrm{mm}$
Air gap thickness	δ	$0.5\,\mathrm{mm}$

[46]. The operating parameters of this prototype are given in Table 1. In addition, radial slots were introduced by [22] into the stator core as an adaptation to the L-PBF production made of metal.

COMSOL's in-built geometry editor is used to design the motor for easy variation of the component parameters. The motor is an externally rotating, permanently excited TFM with three axially arranged phases. Each phase's stator core consists of two identical half-shells containing the winding. For mechanical and thermal reasons, the windings and stator cores are encapsulated in resin. The three stators are mounted on a hollow aluminum shaft, each at an angle of 120° to the other. Figure 2 shows a cut view of the motor geometry, illustrating the different components. Table 2 shows the relevant geometric dimensions of the TFM, which are also depicted in Fig. 3.

Each stator is of the claw pole type with 12 pairs of claw poles per phase. Although the structure of this TFM and a classic claw pole machine appear similar, the mode of operation differs compared to a classic car alternator, for example. In this simulated transverse flux machine, the claw pole geometry is used to obtain a stator with a high number of poles instead of a low-cost, externally excited rotor as in a car alternator. The rotor

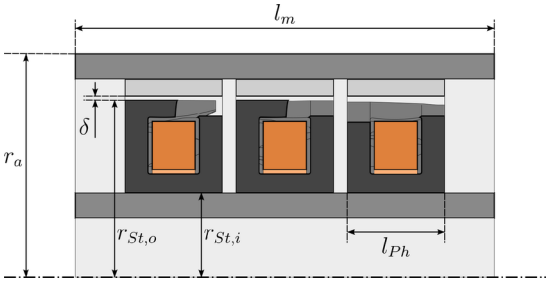

Fig. 3 Cross section of the motor with relevant geometric dimensions as given in Table 2

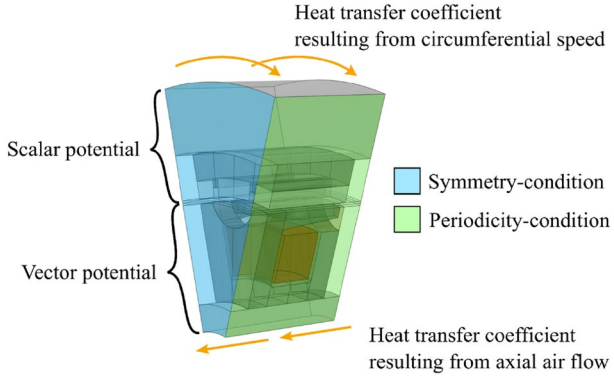

Fig. 4 Simulated section and corresponding electromagnetic modeling and boundary conditions as well as thermal boundary conditions

consists of an aluminum housing into which electrical steel has been inserted. Permanent magnets are located in grooves in the rotor. Due to the very high computational effort of the 3D-FEM simulation, only the smallest periodic section of a single phase (Fig. 4) is considered rather than the entire motor. The simulated section of the machine consists of around 110,000 elements. Figure 5 shows the mesh of the stator core, the rotor and the winding.

The design of the motor allows the application of different symmetry and periodicity conditions. In the axial direction, the model boundaries inhibit a symmetry condition to account for the other motor phases. In tangential direction, a periodicity condition is imposed. This results in a periodic continuation of the modeled section, which in turn results in a complete phase of the motor. For the electromagnetic simulation, both the hollow shaft inside the stator and the cylinder outside the laminated core of the rotor are not taken into account. It is assumed that these non-ferromagnetic parts have a negligible influence, thus reducing the computational effort. All other parts can be divided into two different areas. Where the interaction of electric currents and magnetic fields is important for the simulation, Ampere's law is used. In these areas, the magnetic field is described as a vector field. Due to the computing power, a linear discretization was chosen. These areas of the model include the winding, the stator core and the resin encapsulation. The other areas of the model, in which electrical currents are negligible, are described using magnetic flux conservation. A scalar potential is used there, which reduces the number of degrees of freedom and thus the computational effort. Linear discretization was also chosen in these areas due to the greatly reduced runtime. It is assumed that there are no magnetic interactions between the individual phases, the

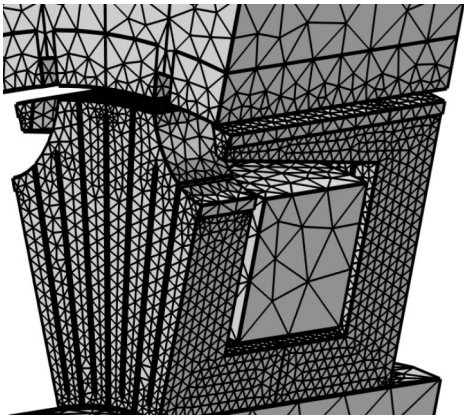

Fig. 5 Mesh of the stator core, rotor and winding. Not shown is the mesh of the resin and the air

stator core and the hollow shaft or the iron plate and rotor housing. Therefore, the interfaces in axial and radial direction are considered as magnetically insulated.

As there is no air exchange between the inside and outside of the complete motor, heat can only be transferred to the environment via the outer surface and the two side surfaces of the rotor, as well as the inside of the hollow shaft. In this case, active air cooling through the hollow shaft is employed in conjunction with natural convection through the outer surface. In real applications, further heat transfer could occur if contact is made with other components via fastenings, shafts or flanges. However, these cannot be taken into account in this work. Since the thermal simulation requires significantly less computational effort, a quadratic discretization was chosen. A uniform temperature distribution of $293\,\mathrm{K}$ is set as the initial condition across the entire model, which can be adjusted in the simulation parameters. Analogous to the electromagnetic conditions, a periodicity condition for the tangential faces of the section are defined for the thermal modeling. The axial boundary surfaces are modeled as adiabatic. This way, the thermal conditions of the phase in the center are met. While this is not accurate for every phase of the TFM due to neglecting of heat transfer on the axial housing surfaces, it is expected for the center phase to operate the hottest and therefore its simulation the most critical. The heat transfer from the rotor to the environment is modeled as a convective heat flow to the surrounding air. The corresponding heat transfer coefficient is calculated using the corresponding circumferential speed of the outer rotor surface. According to [47], the given geometry and velocities result in a laminar flow in the air gap. The ambient air has a pressure of $1.01325\,\mathrm{bar}$ and the previously defined temperature, which is $293\,\mathrm{K}$ per default. The heat transfer coefficient inside the hollow shaft connected to the stator is calculated based on pipe flow with an axial air flow velocity of $2\,\frac{\mathrm{m}}{\mathrm{s}}$. Radiative heat transfer is generally neglected in this simulation.

Most of the material parameters used in this simulation are taken from the COMSOL database. This includes the sintered N38 NdFeB-magnets. For these magnets, a non-linear B-H curve model including coercivity and magnetic coenergy density is used. An exception to the standard materials is the additive manufactured stator core made from iron. For this ferromagnetic material, measurements of physical properties were provided by the Materials Research Institute of Aalen University. Density is $7812\,\frac{\mathrm{kg}}{\mathrm{m}^3}$ and therefore slightly lower than pure iron, possibly due to pores and inclusions created during the manufacturing process. The non-linear magnetization curve is created using

linear interpolation based on 12 measurements. Further information on the magnetic properties of the additive-manufactured material is provided by [24]. To be able to simulate the influence of heating on the operating behavior, the conductivity of the materials with significant electrical current is specified as a function of the temperature. At $20°C$ this is: $\sigma_{Cu} = 6 \cdot 10^7 \frac{\mathrm{S}}{\mathrm{m}}$ for copper [48] and $\sigma_{Fe} = 8.1 \cdot 10^6 \frac{\mathrm{S}}{\mathrm{m}}$ was measured for the additive manufactured iron. In the range of normal operating temperatures, the relationship can be assumed to be linear and calculated using the resistance-temperature coefficient α. For copper, this is

$$\alpha_{Cu} = 3.9 \cdot 10^{-3}\,\mathrm{K}^{-1} \tag{3}$$

and for iron

$$\alpha_{Fe} = 6.57 \cdot 10^{-3}\,\mathrm{K}^{-1} \tag{4}$$

as given in [48]. The temperature-dependent conductivity of the copper winding and stator core are therefore:

$$\sigma_{T,Cu} = (\rho_{Cu} \cdot (1 + \alpha_{Cu} \cdot T))^{-1} \tag{5}$$

$$\sigma_{T,Fe} = (\rho_{Fe} \cdot (1 + \alpha_{Fe} \cdot T))^{-1} \tag{6}$$

3 Calculation of torque and losses

To optimize the motor and calculate the efficiency, it is necessary to simulate the different power losses as accurately as possible. In addition to the copper losses in the windings and the iron losses in the stator, which account for the majority, there are also losses in the rotor laminations and negligible losses in the permanent magnets. There are also mechanical losses in the bearings, seals and due to air resistance. Since these mechanical losses are the same for each geometry variation of the stator, only the stator and winding losses as well as the losses of the rotor's laminated sheet metal core are taken into account.

While calculating the ohmic copper losses is simple, determining the iron losses of the additively manufactured stator core of this TFM is more difficult. One problem lies in the high conductivity of the material and in the approach of reducing the eddy current losses through the shape of the stator and through slots. Unlike the use of electrical steel plates and two-dimensional magnetic flux in conventional motors, in this TFM the slots are oriented differently to the three-dimensional magnetic flux. This results in different levels of eddy current losses in different parts of the stator core. The same magnetization curve in different parts of the stator core can therefore lead to different eddy current losses. If a conventional, empirical model such as the Bertotti model were used to determine the eddy current losses, the coefficients for the individual loss components would have to be measured beforehand. However, as the shape of the stator core is to be changed and optimized, and it is assumed that a change in geometry also affects the eddy currents, this is why the use of such empirical models is not feasible in this case.

To address this issue, it was decided to calculate the different aspects of iron losses in different ways. While hysteresis and excess losses in the stator core are calculated using the Bertotti model, the losses caused by induced eddy currents are simulated directly by 3D-FEM. In the Bertotti model, the eddy currents are proportional to the square of the

electrical frequency (see Eq. 2). This model is based on laminated sheet metal and therefore not able to sufficiently capture the three-dimensional eddy currents occurring in this TFM. By simulating the existing density and direction of currents in the conductive stator core, the effect of geometry changes and the introduction of slots on the eddy currents can be observed and optimized. Based on the simulated currents, the eddy current losses are implicitly derived from resistive heating and are calculated using Ohm's law. All components of the stator's iron losses are then used with the other losses to calculate the motor's efficiency.

The determination of the efficiency was realized with a simulation with several steps in COMSOL. Figure 6 shows a diagram of the simulation process. After the model has been initialized with a stationary study, a dynamic simulation over 60° rotation is carried out first. Since the stator has 12 pole pairs, theoretically a rotation of $360/12 = 30°$ would be sufficient. The reason why the first dynamic rotation covers a rotation by two periodic sections are oscillations of the induced currents, which occur for a very short moment at the beginning of the simulation and decrease with time. The second rotation of the periodic section shows no traces of the oscillations. The course of the magnetic flux density of only the last 30° rotation of this simulation step is used to calculate the hysteresis and excess losses, P_{hy} and P_{ex}, respectively, using the Bertotti model.

The first dynamic simulation also fulfills a function for initializing the second dynamic simulation step. As this means that there is no more oscillation, a simulation of 30° rotation is sufficient. In order to obtain the most accurate results regarding the distribution and density of the induced currents in the stator, the second dynamic simulation is carried out with a significantly smaller step size and tighter tolerances. In addition to the eddy current losses P_{ec} and copper losses P_{Cu}, the losses in the laminated core of the rotor P_{rotor} are also determined in this more precise dynamic simulation using Steinmetz's equation. In addition, the torque is calculated in this step using the Arkkio method and thus the mechanical power P_{mech} is calculated.

By using two consecutive dynamic simulations with different accuracies, a compromise between acceptable runtime and good accuracy of the simulation of the currents can be achieved in this application. The efficiency, which later forms the target function for the optimization, is then calculated as given in Eq. 7.

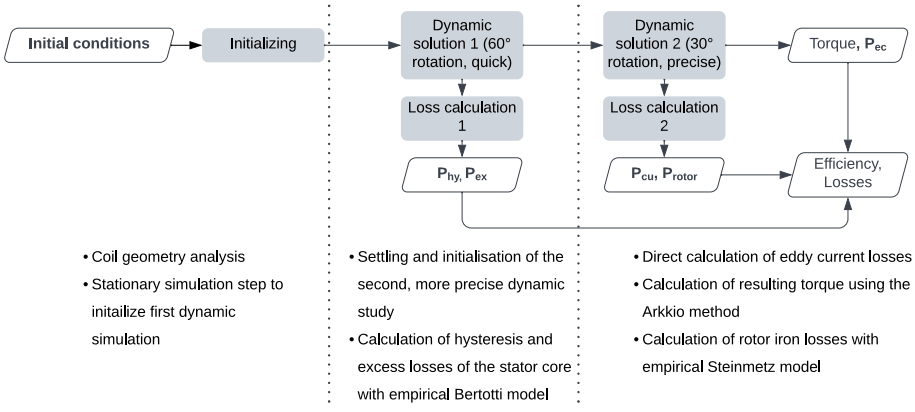

Fig. 6 Flow diagram of the loss calculation consisting of two simulation steps of different accuracy. The first step (Loss calculation 1) is based on a coarser simulation and utilizes empirical models for hysteresis and excess losses, whereas the second step (Loss calculation 2) is based on a finer simulation to accurately calculate the eddy current and rotor losses

$$\eta = \frac{P_{mech}}{P_{mech} + P_{losses}} = \frac{P_{mech}}{P_{mech} + P_{hy} + P_{ec} + P_{ex} + P_{Cu} + P_{rotor}} \tag{7}$$

Up until now, the simulation covers the electromagnetic domain only. Material properties that depend on temperature are assumed constant. In the following chapter, we describe how the thermal domain was taken into account.

4 Coupled thermo-electromagnetic simulation

The heating of electrical machines can not only lead to problems with thermal failure of components, but can also result in a change in material properties. In order to be able to consider not only thermal limit values when optimizing the TFM, but also the efficiency that is achieved when heating occurs during operation, the thermal and electromagnetic parts of the simulation must be coupled. Although it is technically possible to simulate both domains directly coupled, the different simulated time periods cause problems. While the electromagnetic simulation only considers a period of a few milliseconds, a period of minutes to hours must be simulated for the heating. For this reason, the simulation of the physical domains was carried out alternately several times in succession and thus coupled iteratively as shown in Fig. 7.

First, an electromagnetic simulation is carried out as described above (see Fig. 6). From this electromagnetic simulation, the distribution of the two main sources of losses in the stator, eddy current losses and winding losses, as well as the rotor losses are extracted and serve as input for the thermal simulation. By choosing between a steady-state or a transient simulation, it possible to simulate either continuous operation or temporary operation. Steady-state thermal simulations are carried out to calculate the temperature distribution during continuous operation, while transient thermal simulations are used to simulate the heating process of the motor. For both variants, several iterations between thermal and electromagnetic simulation are carried out. In the case of steady-state thermal simulations, the iteration results in a better prediction of the temperature distribution during continuous operation (see Fig. 8a). For transient thermal simulations, an iteration updates the electromagnetic losses after a predefined amount of time, to better reflect the heating process (see Fig. 8b).

Both steady-state and transient thermal simulations are shown in Fig. 8. It was found that for continuous operation, a satisfactory compromise between accuracy and required computing time was achieved after three electromagnetic and three thermal simulations each. Both the coil temperature and the magnet temperature change by less than $0.5\,\mathrm{K}$

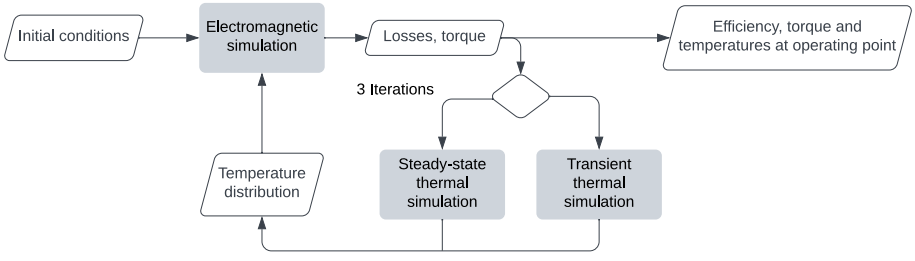

Fig. 7 Flow diagram of the iterative coupling between thermal and electromagnetic domain. The electromagnetic simulation and the loss calculation is carried out according to Fig. 6. The distinction between steady-state and transient thermal simulation is fixed for all iterations

between the third and the fourth iteration. The transient temperature rise shows a slight change in heating after recalculating the losses with the updated temperature distribution. After $180\,\mathrm{s}$ of operation, the temperatures are still increasing. However, the transient simulation can be consulted to examine the maximum temperatures after a certain amount of time, compared to the continuous operation in the steady-state simulation.

5 Simulation results

The simulation of the operating behavior of the TFM with three electromagnetic and three thermal simulations takes around 50 min on a 6-core desktop workstation.

The following values were simulated for the original geometry of the stator for the operating point of $1600\,\mathrm{min}^{-1}$ rotational speed and a current of $4\,\mathrm{A}$ at room temperature. The calculated torque was $0.266\,\mathrm{Nm}$. The distribution of the magnetic flux density shows values in areas of the teeth of the stator core that lie outside the saturation magnetization of the material used. This behavior can be explained by the relatively low quality of the mesh elements at this point due to the very sharp geometry.

These elements lie in an area that is subsequently varied and changed during optimization, which is why it is not possible to round off or change the transition of the slots through the stator tooth. Since only very few elements are involved and the magnetization is only slightly higher than the saturation magnetization, the influence of this inaccuracy on the overall result is assumed to be negligible. All other areas of the model show a plausible magnetic flux density as shown in Fig. 9.

The distribution of the currents is shown in Fig. 10. It illustrates how the induced eddy currents spread in a spiral in the areas of the stator core divided by the slots. The strongest currents are located in the stator teeth close to the air gap, likely induced by the permanent magnets moving close-by.

Furthermore, there are increased currents around the upper ends of the slots. Figure 11 shows the power loss distribution averaged over one electric period. As already shown for the currents, the average power loss during rotation is also higher in the vicinity of the air gap. There are also higher power losses above the slots and in the inner corners.

The design of the motor with a stator made of additively manufactured iron generates unusually high eddy current losses, which significantly reduce the efficiency. The

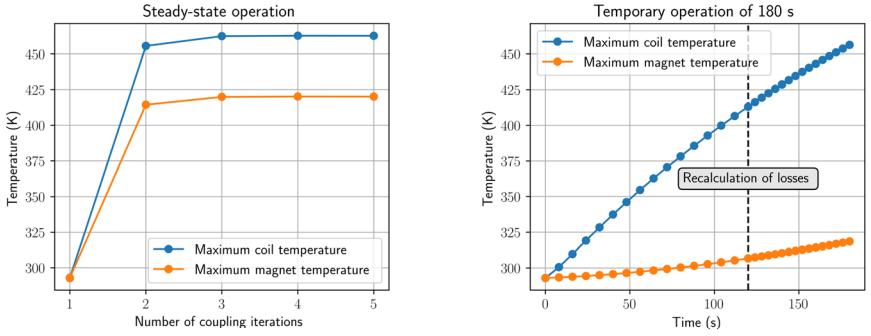

(a) Temperatures during steady-state operation after each coupling iteration

(b) Temperature rise during temporary operation of 180 s with a loss recalculation after 120 s

Fig. 8 Comparison between temperatures after steady state operation and temporary operation. It can be seen that the temperatures in steady-state operation converge after 3 iterations. For temporary operation the temperatures still rise after 180 s

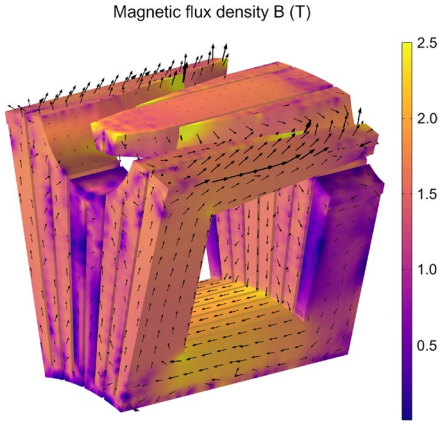

Fig. 9 Momentary image of the magnetic flux density, showing magnitude and orientation

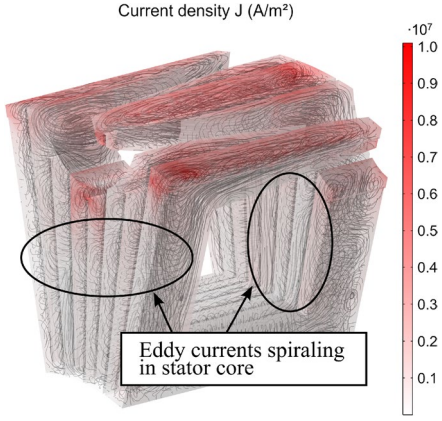

Fig. 10 Momentary image of the eddy currents. Shown in black are the eddy currents' trajectories, in red the magnitude of the local current density. The eddy currents curl in the regions separated by the slots and are strongest in the red areas near the teeth of the stator core

exceptionally high losses in the stator core in particular result in a comparatively poor efficiency of around $45.7\,\%$. These losses result in a heating of the stator.

Figure 12 shows the temperature distribution of the simulated motor section and stator core after $28\,\mathrm{s}$ of operation. It can clearly be seen that the fastest heating takes place at the teeth of the stator core. The windings initially remain colder than the stator core surrounding them and there is only a small amount of heat transfer through the air gap to the rotor. At a rotational speed of $900\,\mathrm{min}^{-1}$ and $0.6\,\mathrm{Nm}$ torque, the difference in efficiency between constant material properties and temperature dependent material properties amounts to over $5\,\%\mathrm{pt}.$ (see Table 7 for more detailed results).

The influence of the temperature change on this motor is significant due to the comparatively high conductivity of the stator core. In addition, the temperature dependence of the conductivity of iron is significantly higher than that of copper, for example. Without a coupled simulation and consideration of the temperature change, the simulation results for this motor would significantly differ. Therefore, a coupling between the electromagnetic and thermal domain is necessary to accurately predict the motor's efficiency. This is essential for the following design optimization of the stator core.

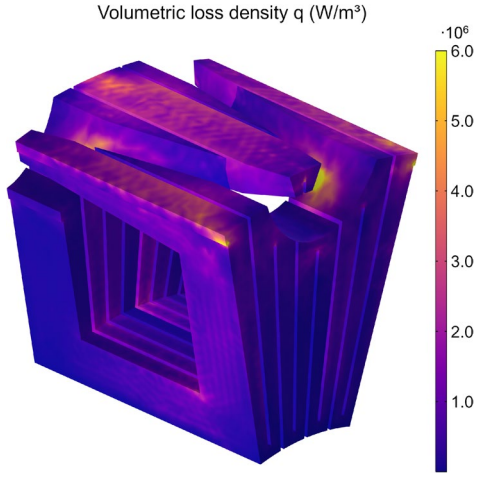

Fig. 11 Loss density averaged over one electrical period. Notice the higher losses in the stator teeth

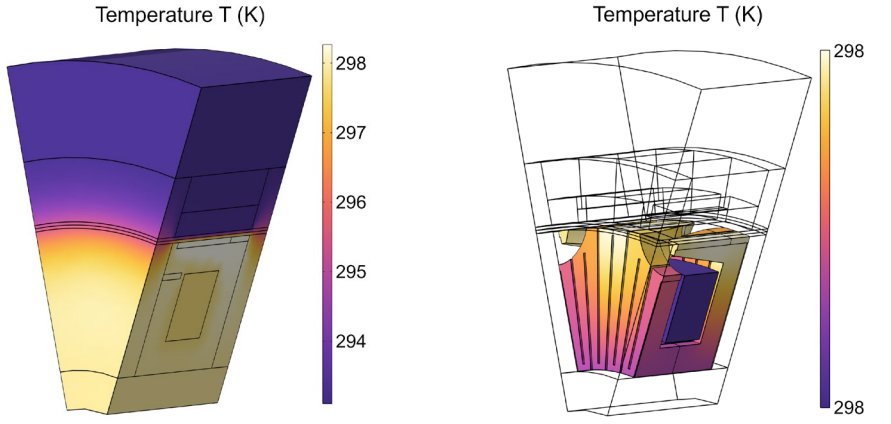

(a) Temperature distribution in simulated section (b) Temperature distribution in stator and coil

Fig. 12 Temperature distribution after 28 s of operation

6 Stator core design optimization

The coupled simulation model can be used to optimize the shape of various engine components for different target values and operating points. In this work, the shape of the teeth of the additively manufactured stator core is to be optimized for maximum efficiency after a timed operation of 3 min. Thermal limit values for the temperature of the winding and the permanent magnets must not be exceeded. Three parameters were varied to optimize the shape of the stator. Namely the length of the teeth, the width of the tooth tip and the depth of the cut-out between the teeth. The original geometry of the stator core is shown in Fig. 13 in addition to a graphical representation of the optimization parameters (see also Table 3 for parameter values). The aim of the optimization was to achieve a compromise between saturation magnetization, magnetic flux leakage between the teeth and minimization of eddy current losses in the area of the air gap in order to maximize the efficiency.

The derivative-free Nelder-Mead method was employed for parametric optimization. This method allows for the use of the complexly calculated efficiency as a target function and arbitrary design parameters. An optimality tolerance of 0.001 or 28 iterations was

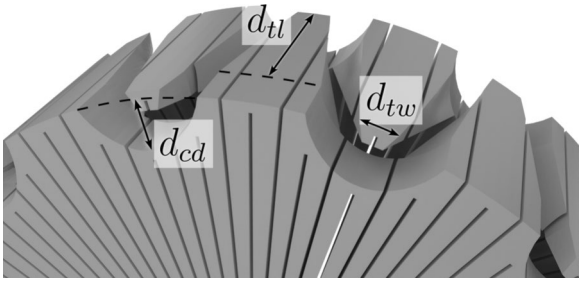

Fig. 13 Original stator geometry as designed for SMC including the parameters varied during optimization

Table 3 Parameters for the optimization and their respective bounds

Parameter	Lower bound	Upper bound	Initial value
Cutout depth d_{cd}	2	7	5
Tooth length d_{tl}	3	10	4
Tip width d_{tw}	0.2	4	2

All values are in mm

selected as the stopping criterion. Due to the long runtime of the simulation and only three parameters to be optimized, this was deemed sufficient. The parameters and their respective lower and upper bounds are given in Table 3. A maximum winding temperature of $425\,\mathrm{K}$ for the stator and a maximum magnet temperature of $350\,\mathrm{K}$ for the rotor were defined as thermal constraints. These limits are intended to allow the use of class F insulation in accordance with DIN EN 60085 [49] and regular neodymium permanent magnets of temperature class N. The initial set of parameters was selected to ensure that thermal limits would not be exceeded. The original shape of the stator core originates from a previous research project and was designed for the use of soft magnetic composites (SMC). The optimal shape might therefore differ when considering an additively manufactured stator core.

In order to investigate the influence of the choice of operating point and the effect of the coupled thermal-electromagnetic consideration, two optimizations runs at different operating points were carried out. One so-called low-speed optimization at $300\,\mathrm{min}^{-1}$ and a so-called high-speed optimization at $1600\,\mathrm{min}^{-1}$ rotational speed. During both runs, the current was set to $4\,\mathrm{A}$. Figure 14 shows the course of optimization of the three parameters for both operating points. The initial geometry and the first three optimization steps of the Nelder-Mead algorithm are the same for both optimization runs. After around 10 iterations, the optimizations begin to converge at different points in the parameter space. The optimized parameters are given in Table 4.

The resulting geometry of the low-speed variant is shown in Fig. 15. The stator geometry generated by the optimization for low speeds differs only slightly from the original geometry. The width of the tooth tips and the length of the teeth is slightly larger, while the cut-out in the stator core between the teeth is significantly deeper. The deeper cut-out removes material that contributes very little to torque generation, but still causes iron losses. The volume therefore decreased by $11.7\,\%$ from $6.05\,\mathrm{cm}^3$ to $5.34\,\mathrm{cm}^3$.

The stator geometry after optimization for a high speed of $1600\,\mathrm{min}^{-1}$, however, differs significantly from the original geometry as shown in Fig. 16. The teeth are significantly shorter, with wider tips and a deeper cut-out between the teeth. The volume is reduced by $16.2\,\%$ to $5.065\,\mathrm{cm}^3$.

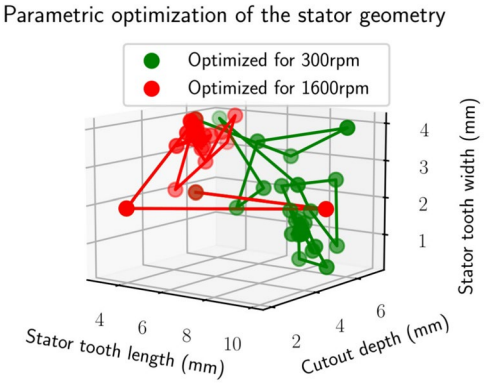

Fig. 14 Parametric optimization and convergence for different rotational speeds

Table 4 Parameter sets of both optimized variants

Parameter	Low-speed variant	High-speed variant
Cutout depth (mm)	6.00	5.07
Tooth length (mm)	8.67	4.47
Tip width (mm)	2.56	2.88

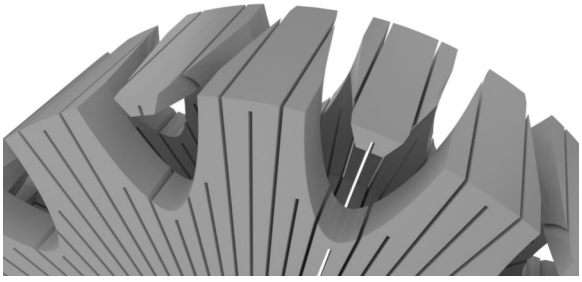

Fig. 15 Stator geometry optimized for $300\,\mathrm{min}^{-1}$

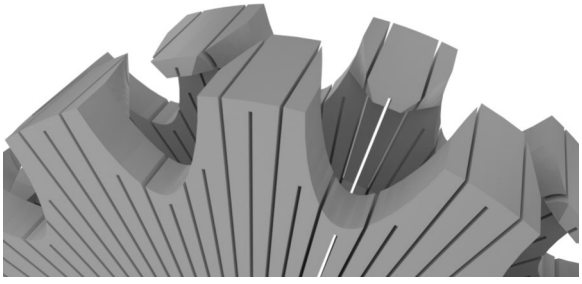

Fig. 16 Stator geometry optimized for $1600\,\mathrm{min}^{-1}$

Efficiency maps were created to analyze the effects of the different stator shapes for different operating conditions. Since the torque is not yet known before the simulation, the various operating points were defined with predefined speed and current values. For this purpose, 45 points between 150 and $1620\,\mathrm{min}^{-1}$ and for currents between 1 and $10\,\mathrm{A}$ were defined. The different geometries of the motor can have different torques for the same specified current. This means that the interpolation points of the map for different geometries of the motor are positioned at different points in the efficiency map.

To visualize differences between two maps cleanly, cubic interpolation was performed between the interpolation points of each motor geometry.

Firstly, the efficiency map of the motor with the original stator geometry was formed as a starting point (Fig. 17). This is intended to show the characteristics of the TFM with a slotted, additively manufactured stator core. On the other hand, it serves as a reference for comparing and assessing the performance of the two optimized stator cores. The efficiency of the analyzed motor is comparatively low and has its maximum at low speeds and high torque.

To visualize the differences between the optimized geometries of the motor, the difference in efficiency compared to the original geometry is shown in Figs. 18 and 19 for the low-speed and high-speed variant, respectively. A positive value corresponds to an improvement of the optimized variant compared to the original geometry. The support points of the optimized variants are each shown as a dot, those of the original geometry as a cross.

The variant of the motor which was optimized for the operating point of $300\,\mathrm{min}^{-1}$ at $4\,\mathrm{A}$ current shows an improvement in the area with low speeds and high torque, which decreases with increasing speed. For higher speeds and low torques there is no relevant difference in efficiency compared to the original geometry.

The variant optimized for high speeds shows an improvement over large area of operating conditions. Only a small range at low speed and medium to high torque results in a reduced efficiency compared to the original geometry. The efficiency gain at the target operating point measures $+4.15\,\%\mathrm{pt.}$, while the maximum of improvement is in the range of medium speed and low to medium torque. Both results verify the optimization process. The optimized geometries offer an increased efficiency in their respective operating points. It should also be noted that, beyond the improvements at the designated operating points, both variants demonstrate enhanced efficiency over a substantial portion of the efficiency map. For both variants, the maximum efficiency increase is achieved at operating conditions different from their respective target points.

For further investigation into the different characteristics of the two optimized variants of the TFM, diagrams of the different power losses were drawn up. Figure 20 shows the difference of copper losses between the low-speed variant and the high-speed

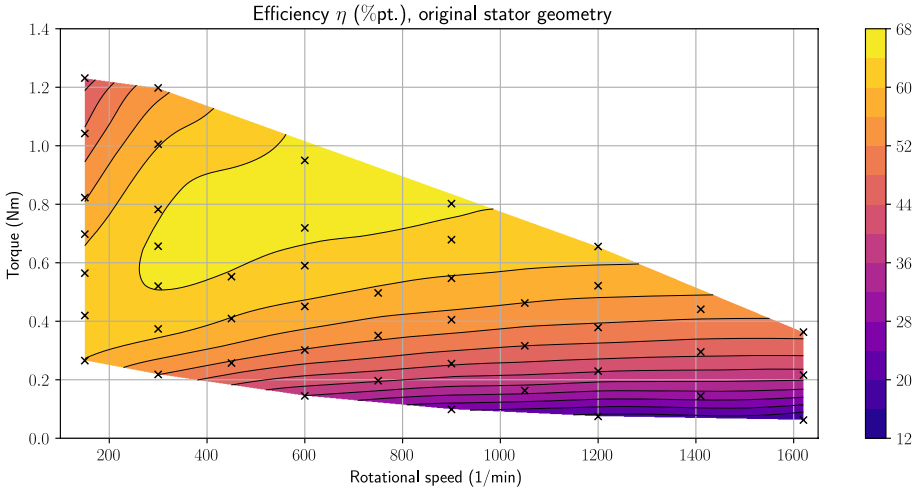

Fig. 17 Efficiency map of the original stator geometry

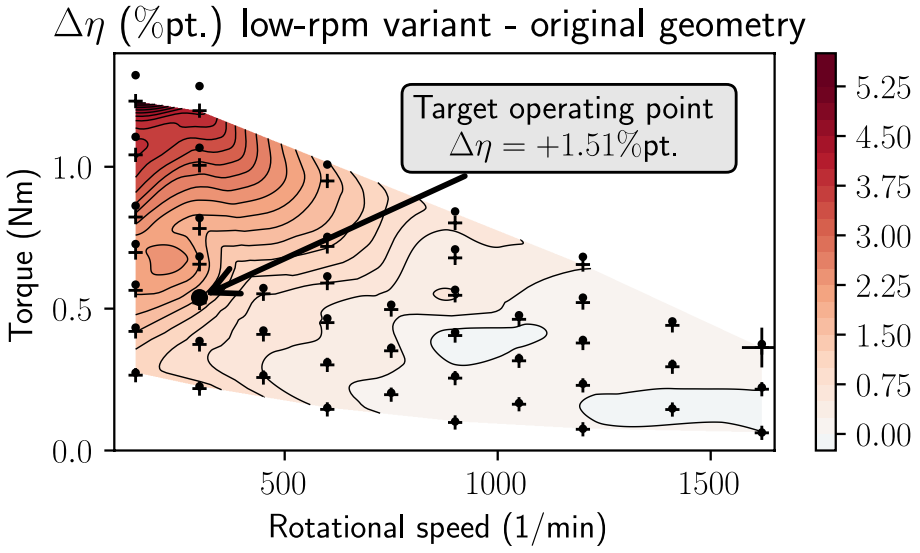

Fig. 18 Difference in efficiency between the stator optimized for low rpm and the original stator geometry. The optimized variant shows higher efficiency towards low-speed high-torque operation

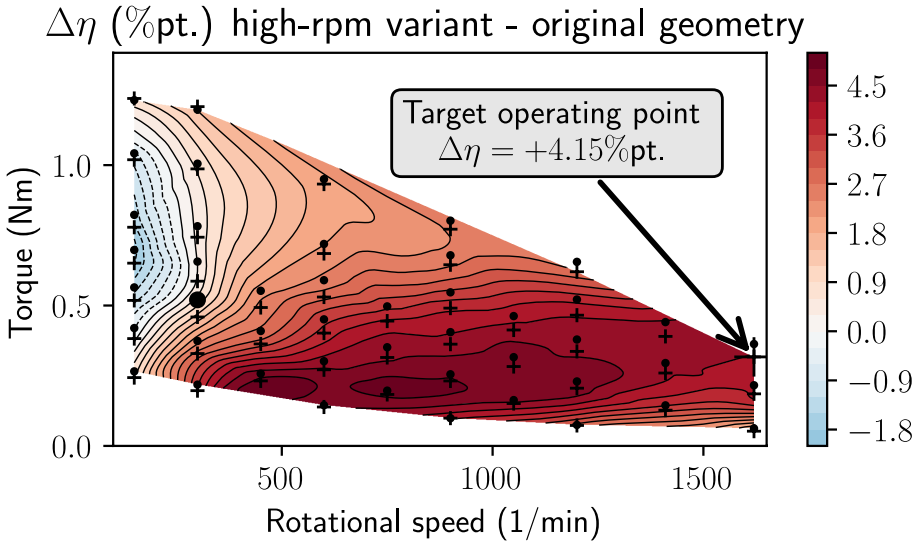

Fig. 19 Difference in efficiency between the stator optimized for high rpm and the original stator geometry. The optimized variant shows higher efficiency towards mid- to high-speed operation

variant. A negative value (shaded in blue) corresponds to a lower copper loss of the low-speed variant.

The copper losses of the motor are only dependent on the current and, to a lesser extent, the temperature. However, due to the very different shape of the stator core of the two optimized variants, different currents are required to achieve the same torque. This means that the copper losses are also different for the same operating points. The plot clearly shows that the low-speed variant of the TFM has lower copper losses for the same operating point than the high-speed variant. In other words, the torque for the same current is higher for the low-speed variant than for the high-speed variant. The higher the torque, the greater the difference in copper losses between the two optimized variants of the motor. This is due to the different amount of iron material in the stator.

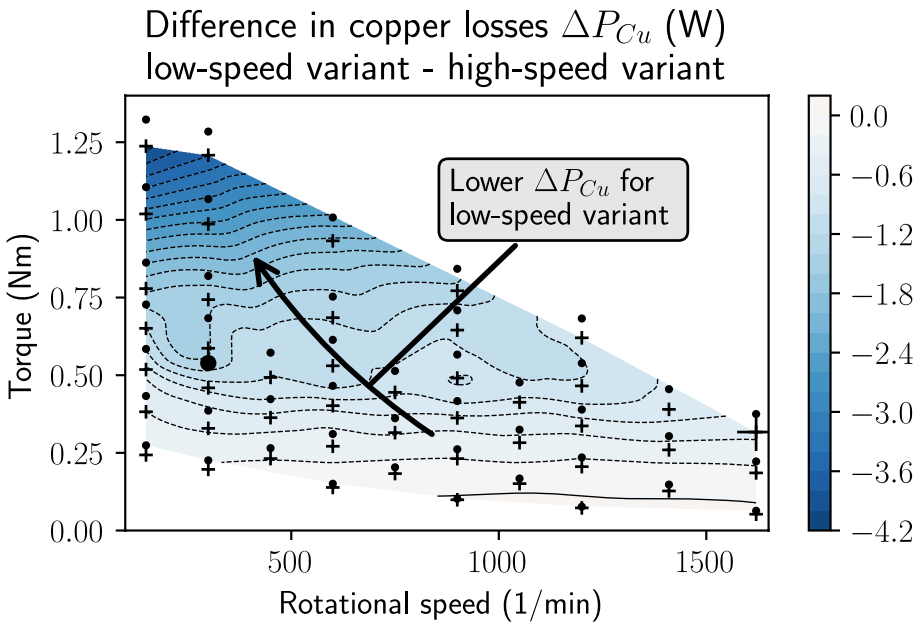

Fig. 20 Difference in copper losses between stator geometry optimized for high rpm and for low rpm. Dots and crosses indicate the support points of low-speed and high-speed variant, respectively. The variant optimized for low speeds exhibits reduced copper losses towards low-speed, high-torque operation compared to the high-speed variant

The variant which was optimized for low speeds has significantly larger stator teeth and slightly smaller recesses between the teeth. These ensure higher magnetic conductivity and lower magnetic saturation of the material. Consequently, a higher magnetic flux Φ and thus a greater torque is achieved with the same current.

Similarly, the iron losses of the stator, i.e., eddy current, hysteresis and excess losses, of the two optimized variants can also be compared. The plot shown in Fig. 21 shows the difference of iron losses between the low-speed variant and the high-speed variant. Positive values (shaded in blue) therefore indicate lower iron losses for the high-speed variant.

It can be seen that the high-speed variant has lower iron losses over the entire map compared to the low-speed variant, but in contrast to the copper losses, this difference increases mainly with increasing speed. This behavior is also expected and plausible, as the low-speed variant of the motor has higher losses in hysteresis, excess and, above all, eddy currents due to the larger, more voluminous stator teeth. The non-uniform magnetic field of the moving permanent magnets results in a higher harmonic excitation and two-dimensional, rotating magnetization, particularly in the vicinity of the air gap where the stator teeth are located. These effects have a particularly strong influence of the amount of iron in the teeth on the total iron losses in this area. Due to the shorter and narrower teeth of the stator of the high-speed variant, significantly lower iron losses as seen in the plot are expected.

When optimizing the stator geometry, however, the target function was not the only requirement, but also compliance with thermal limit values after $3\,\mathrm{min}$ of operation at the respective operating point. In order to show the differences in the thermal behavior of the two motor geometries, the difference in the maximum winding temperature is displayed on a torque/speed map in Fig. 22. A positive value corresponds to a higher

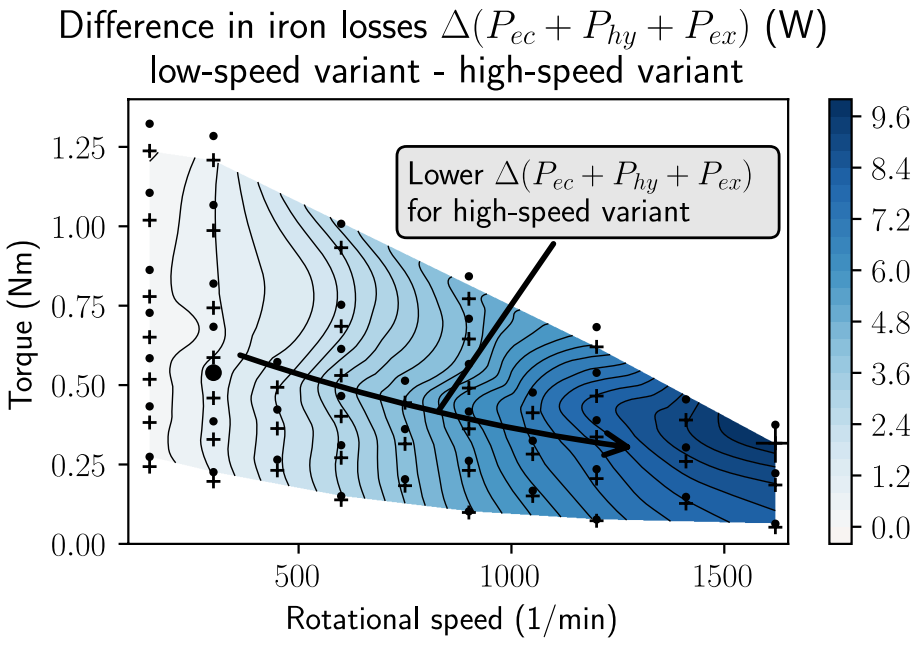

Fig. 21 Difference in iron losses between stator geometry optimized for high rpm and for low rpm. Dots and crosses indicate the support points of low-speed and high-speed variant, respectively. The variant optimized for high speeds shows lower iron losses towards higher speeds compared to the low-speed variant

temperature of the geometry which was optimized for lower speeds. The low-speed geometry cannot reach all areas of the map without exceeding the thermal limit.

As expected from the power loss plots, the variant of the TFM optimized for high speed heats up significantly less in this range than the low-speed variant. The thermal limit value of the winding of $425\,\mathrm{K}$ is already exceeded by the low-speed geometry from around $1480\,\mathrm{min}^{-1}$, while operation in the entire characteristic map is possible with the high-speed geometry.

The level of losses, efficiency and critical temperatures in the rotor and stator of the different variants of the motor can be compared for the final analysis for the two points of optimization. The first consideration is for the operating point at $300\,\mathrm{min}^{-1}$ and $0.58\,\mathrm{Nm}$. A second comparison for higher speeds was done at the operating point of $1600\,\mathrm{min}^{-1}$ and $0.4\,\mathrm{Nm}$ (Tables 5 and 6).

It can be seen that the weighting of the different types of losses differs greatly for both operating points. As previously stated, the iron losses are particularly dependent on the speed, while the copper losses are particularly dependent on the torque. The result of the optimization is plausible in this respect. At low speeds, the iron losses account for almost half of the total losses. The larger stator teeth reduce the copper losses by almost $8\,\%$, while the slight increase in iron losses at low speeds has only a minor effect. The efficiency of the motor variant optimized for this operating point is around $2\,\%$ higher than that of the original geometry.

At the operating point at high speeds, the iron losses clearly predominate. The variant of the motor that was optimized for this operating point has $15.6\,\%$ lower iron losses than the original geometry due to the significantly shorter, smaller stator teeth. As the copper losses only have a minor influence at high speeds, the slightly higher values only make a small difference. The efficiency is around $8\,\%$ higher than the original geometry of the TFM.

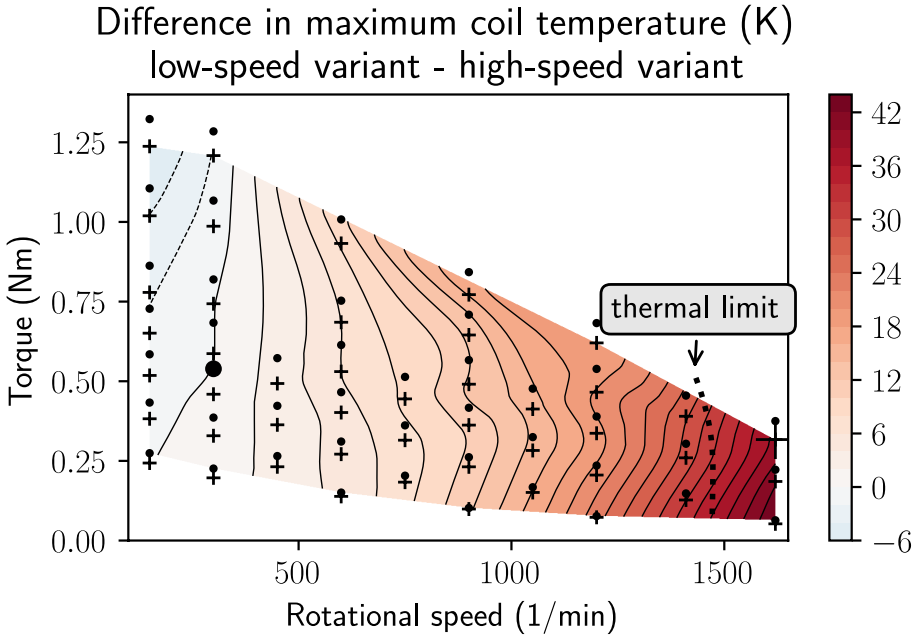

Fig. 22 Difference in maximum coil temperature between stator geometry optimized for high rpm and for low rpm. Dots and crosses indicate the support points of low-speed and high-speed variant, respectively. The variant optimized for low speeds reaches higher temperatures towards higher speeds compared to the high-speed variant. The thermal limit of $425\,\mathrm{K}$ even limits operation at speeds above around $1480\,\mathrm{min}^{-1}$ for the low-speed variant

Table 5 Comparison of optimization results at $300\,\mathrm{min}^{-1}$ and $0.58\,\mathrm{Nm}$

	Original stator geometry	Optimized for low speed	Optimized for high speed
P_{ec} (W)	2.864	2.917	2.222
P_{hy} (W)	2.493	2.305	2.072
P_{Cu} (W)	4.461	4.138	5.514
P_{losses} (W)	9.818	9.360	9.808
T_{Cu} (K)	308.677	307.554	307.649
η (%)	64.947	66.305	65.073

Even though the high-speed variant was not optimized for this operating point, it still shows a higher efficiency and also lower coil temperature compared to the original geometry

Table 6 Comparison of optimization results at $1600\,\mathrm{min}^{-1}$ and $0.4\,\mathrm{Nm}$

	Original stator geometry	Optimized for low speed	Optimized for high speed
P_{ec} (W)	43.926	44.830	35.928
P_{hy} (W)	13.052	12.160	10.842
P_{Cu} (W)	6.195	5.932	6.711
P_{losses} (W)	63.173	62.922	53.481
T_{Cu} (K)	448.474	448.499	412.277
η (%)	51.599	51.647	55.966

Again, the low-speed variant which was not optimized for this operating point still shows an increase in efficiency compared to the original geometry. The high-speed variant shows a significantly lower coil temperature due to reduced eddy current losses

It is interesting to note that both variants of the motor, which have not been optimized for the respective operating point, nonetheless exhibit a slightly enhanced efficiency compared to the original geometry. This cannot be explained by an optimum adaptation to the respective speed, but rather by a generally better adapted shape of the stator core.

Table 7 Comparison of optimization results at $900\,\mathrm{min}^{-1}$ and $0.6\,\mathrm{Nm}$ between room temperature (T=*const.*) and taking temperature changes into account (T=*var.*)

	Original stator geometry		**Optimized for low speed**		**Optimized for high speed**	
	T=*const.*	**T=*var.***	**T=*const.***	**T=*var.***	**T=*const.***	**T=*var.***
P_{ec} (W)	28.955	22.561	29.505	23.201	22.475	18.799
P_{hy} (W)	7.679	8.198	7.170	7.627	6.210	6.666
P_{Cu} (W)	7.788	8.264	7.302	7.654	7.874	8.722
P_{losses} (W)	44.422	39.023	43.977	38.482	36.559	34.187
η (%)	55.975	60.980	56.170	61.335	60.681	64.073

The differences in efficiency indicate a strong influence of the temperature on the electromagnetic behavior

Furthermore it can be seen that the hysteresis losses of the variant optimized for low speeds are lower than those of the original geometry, while the eddy current losses increase. One explanation for this is that the total volume of the stator core is smaller, but the surface area of the stator teeth near the air gap is larger. Due to rotating magnetization and higher harmonic excitation caused by the non-uniform field of the permanent magnets, the eddy current losses are greater in this area However, these effects are not taken into account in the Bertotti model for calculating the hysteresis and excess losses.

Finally, in order to evaluate the influence of the consideration of temperature in the simulation, we compared operation at a prescribed temperature of $293\,\mathrm{K}$ with steady-state operation taking the temperature rise into account. The original geometry was compared as well as both the low-speed and the high-speed variant. The operating point in each simulation is $900\,\mathrm{min}^{-1}$ and $0.6\,\mathrm{Nm}$. The results are given in Table 7.

For this motor, which has a relatively high conductivity of the stator core, the operating behavior is strongly dependent on the temperature. As the conductivity of the additively manufactured stator core decreases with increasing temperature, the eddy current losses decrease as the temperature rises. As the eddy current losses make up the majority of the losses at most operating points, the efficiency of this TFM increases as the temperature rises. The strong difference between the results with and without consideration of the heating clearly shows the necessity of the coupled electromagnetic-thermal simulation in this application.

7 Conclusion

In this work a coupled electromagnetic-thermal simulation model of a transverse flux machine was constructed. This simulation model was then utilized to optimize the geometry of the stator core for different operating points. It was shown that the multi-step simulation makes it possible to consider various coupled physical effects together with the appropriate accuracy and level of detail for the application. The eddy current losses are simulated directly using a 3D-FEM simulation, which accounts for the influence of the complex geometry. In contrast to this detailed modeling, hysteresis and excess losses in the stator core are determined using the simpler empirical Bertotti method.

The iteratively coupled electromagnetic-thermal simulation also makes it possible to simulate different time spans of the two domains and achieve accurate results with just a few iterations. When designing this TFM, the interaction between the electromagnetic

losses on the thermal behavior and the temperature on the operating behavior can be taken into account in order to optimize it for real operating conditions.

The coupled simulation enables the consideration of thermal limit values or a weighting between several thermal, electromagnetic and mechanical objective functions, e.g., maximum torque density with minimum heating. Due to the gradient-free optimization algorithm, the objective function can easily be extended to include weight and/or volume. The presented method allows not only the optimization of the geometry of the stator core, but also any combination of parameters for any component. In this example, the efficiency was optimized for two different operating points, taking into account thermal limit values for the winding and magnets. The design variables were three geometric parameters of the stator core. Although this number of design variables is comparatively low, the optimization still provided promising results. The result show that both optimizations are significantly more efficient at the respective operating point than the original geometry of the TFM. These improvements are the result of physically plausible changes to the shape of the stator core. Particularly during operation with higher power, it becomes apparent that only the variant of the motor that was optimized for this purpose is able to complete the specified operation without exceeding the thermal limits.

A comparison of the simulation results with and without coupled consideration of the temperature change shows a significant difference for this TFM. The strong interactions between the temperature and especially the eddy current losses make a coupled simulation of both domains necessary in order to obtain accurate, meaningful results.

Compared to existing approaches in TFM optimization, the presented approach introduces several key advancements. Most previous studies either rely on purely electromagnetic models or use simplified thermal representations, which limits the accuracy when strong temperature-dependent loss mechanisms are present. In contrast, the proposed iteratively coupled electromagnetic-thermal approach captures the nonlinear interaction between eddy current losses, material properties, and thermal boundary conditions with substantially higher fidelity. Another important improvement is the combination of detailed 3D-FEM loss calculation with a computationally efficient surrogate for hysteresis and excess losses, enabling both accuracy and practical runtimes. The multi-step simulation procedure also reduces numerical oscillations and improves robustness during the simulation of different operating points, which is essential for further optimization. Finally, integrating this high-fidelity model into a gradient-free optimization method represents a step forward, as it allows the direct use of complex, non-differentiable FEM outputs and enables the optimization of theoretically arbitrary parameters.

8 Discussion and outlook

The results of the simulation and optimization are primarily intended to demonstrate the function and advantages of the developed method. For the two operating points considered in this work a good convergence was observed. Future works for different operating points must confirm and validate the convergence of the iterative simulation method. As there was often insufficient information available regarding the specific operating environment and the design of the TFM at this stage of development, some assumptions and simplifications were made for the simulation model. The assumptions taken for boundary conditions such as the stator and rotor cooling are based on values of a previous machine. The developed method however is independent of the precise

values of boundary conditions. For future application of this multi-step and multidisciplinary simulation and optimization method, the relevant boundary conditions for all involved physical domains must be known.

In addition, physical testing is required to validate and verify the simulation models. This includes the validation of the geometry by comparing the optimized geometry with the manufactured parts, as well as a validation of key performance indicators. These indicators can range from global measures such as efficiency or maximum temperature down to more detailed measures as e.g., the anisotropic thermal conductivity or the response ratio for the magnetic analysis as presented by [24]. By validating multiple performance indicators, the multidisciplinary aspect of the results from this optimization method can be addressed.

Future works include the implementation of a more sophisticated thermal model for e.g. active liquid cooling of the TFM to increase the power, and physical testing to validate the simulation models. Since decisions regarding materials, joining methods and possible openings in the rotor have a major influence on the thermal model, it is essential that these changes are adapted in the simulation model during the course of development. The temperature dependence of the hysteresis loops of the soft magnetic materials could also be taken into account, as well as possible losses of the permanent magnets. The results also suggest that the use of the unmodified Bertotti model does not provide optimal accuracy for magnetization with rotating and higher harmonic components.

While this work focused on the optimization with regard to the motor's efficiency, future works can take other aspects into account, such as torque ripple, structural integrity or lightweight design. The multidisciplinary gradient-free optimization approach offers the potential to include multiple aspects in the objective function. However, challenges could arise when the presented method is applied to different optimization problems, as the simulation model was constructed with the aim of optimizing the efficiency in mind. If other multidisciplinary effects will be taken into account, the simulation model might require adaptations to capture the relevant effects such as a two-way coupling between the electromagnetic and the structural domain. Furthermore, an increased number of design variables widens the parameter space, offering more geometric freedom and potentially larger improvements compared to the baseline geometry. This comes at a higher computational cost, however. A trade-off between geometric freedom, simulation accuracy and computational cost must be accepted.

The presented method is not limited to the simulation and optimization of TFM, but can also be applied for other types of electrical machines. However, the significantly higher cost of the electromagnetic-thermal coupled simulation is probably only justified if there is a comparatively strong interaction between the two domains.

Acknowledgements
The authors would like to sincerely thank Julian Schurr, M.Sc., and Prof. Dr. Dagmar Goll from Aalen University for providing the measured material properties essential for setting up the simulation model. Their valuable contributions and support have significantly enhanced the quality of this research.

Replication of results
The simulation and optimization results can be replicated with COMSOL Multiphysics 6.1. All necessary parameters and boundary conditions are provided in the article. Additional data can be provided upon reasonable request.

Author contributions
Conceptualization: Simon Knecht; Methodology: Simon Knecht, Tim Lefringhausen; Formal analysis and investigation: Tim Lefringhausen; Writing - original draft preparation: Simon Knecht, Tim Lefringhausen; Writing - review and editing: Simon Knecht, Tim Lefringhausen; Funding acquisition: Albert Albers, Nejila Parspour; Resources: Albert Albers; Supervision: Albert Albers, Nejila Parspour.

Funding
Open Access funding enabled and organized by Projekt DEAL. This study was funded by the Ministry of Science, Research and Arts of the Federal State of Baden-Württemberg within the InnovationCampus Future Mobility (ICM) under Grant number EM8 – FutureM.

Data availability
The data that support the findings of this manuscript are available from the corresponding author upon reasonable request.

Declarations

Ethics approval and consent to participate
Not applicable.

Consent for publication
All authors have read and agreed to the published version of the manuscript. This manuscript does not contain any individual person's data in any form (including identifiable images or personal information); therefore, consent for publication is not applicable.

Competing interests
The authors declare no competing interests.

Received: 29 August 2025 / Accepted: 3 February 2026
Published online: 24 February 2026

References

1. Fischer R, Nolle E. Elektrische Maschinen: Aufbau, Wirkungsweise und Betriebsverhalten, 18, neu bearbeitete. auflage. München: Hanser; 2022.
2. Kaiser B, Parspour N. Transverse flux machine–a review. IEEE Access. 2022;10:18395–419. https://doi.org/10.1109/ACCESS.2022.3150905.
3. Ahn H, Jang G, Chang J, Chung S, Kang D. Reduction of the torque ripple and magnetic force of a rotatory two-phase transverse flux machine using herringbone teeth. IEEE Trans Magn. 2008;44(11):4066–9. https://doi.org/10.1109/TMAG.2008.2001586.
4. Binder A. Elektrische Maschinen und Antriebe. Springer Berlin Heidelberg, Berlin, Heidelberg; 2017. https://doi.org/10.1007/978-3-662-53241-6.
5. Schröder D. Elektrische Antriebe - Grundlagen. Springer Berlin Heidelberg, Berlin, Heidelberg 2013. https://doi.org/10.1007/978-3-642-30471-2.
6. Keller M. Entwurf Einer Permanentmagnetisch Erregten Transversalflussmaschine aus Pulververbundwerkstoff Für Robotikanwendungen, 1. auflage edn. Berichte aus dem Institut für Elektrische Energiewandlung, 2019;8. Shaker, Düren.
7. Schmid A. Transversalflussmaschine in axialer anordnung. PhD thesis, Montanuniversität Leoben 2012.
8. Parspour N. Novel drive for use in electrical vehicles. In: 2005 IEEE 61st vehicular technology conference, 2005;2930–2933. IEEE, Stockholm, Sweden. https://doi.org/10.1109/VETECS.2005.1543883.
9. Baker NJ, Atkinson GJ, Washington JG, Mecrow BC, Nord G, Sjoberg L. Design of high torque traction motors for automotive applications using modulated pole smc machines. In: 6th IET international conference on power electronics, machines and drives (PEMD 2012), 21–21. IET, Bristol, UK, 2012. https://doi.org/10.1049/cp.2012.0311.
10. Hackmann W, Binder A. Aussenläufer-transversalflussmaschinen für radnabenantriebe in straßenbahnen. In: Elektrisch-Mechanische Antriebssysteme: Innovationen - Trends - Mechatronik. Energietechnische Gesellschaft im VDE (ETG) und VDI-Gesellschaft Entwicklung Konstruktion Vertrieb in Zusammenarbeit mit VDMA/FVA, Fulda 2004. http://tubiblio.ulb.tu-darmstadt.de/24528/.
11. Jung J, Ulbrich S, Hofmann W. Design process of a high torque density direct drive involving a transverse flux machine. In: 2014 International conference on electrical machines (ICEM), 1096–1102. IEEE, Berlin, Germany 2014. https://doi.org/10.1109/ICELMACH.2014.6960318.
12. Elantably AMA. An approach to sizing high power density tfpm intended for hybrid bus electric propulsion. Electric Mach Power Syst. 2000;28(4):341–54. https://doi.org/10.1080/073135600268306.
13. Mitcham AJ. Transverse flux motors for electric propulsion of ships. In: IEE colloquium on new topologies for permanent magnet machines, 1997;3. IEE, London, UK. https://doi.org/10.1049/ic:19970520.
14. Baker NJ, Jordan S. Comparison of two transverse flux machines for an aerospace application. IEEE Trans Ind Appl. 2018;54(6):5783–90. https://doi.org/10.1109/TIA.2018.2849737.
15. Mecrow BC. High torque machines for power hand tool applications. In: International conference on power electronics machines and drives, 2002;644–649. IEE, Bath, UK. https://doi.org/10.1049/cp:20020192.
16. Kumar R, Zhu Z-Q, Duke A, Thomas A, Clark R, Azar Z, et al. A review on transverse flux permanent magnet machines for wind power applications. IEEE Access. 2020;8:216543–65. https://doi.org/10.1109/ACCESS.2020.3041217.
17. Mordey WM. Electric Generator. US Patent 1890;437,501.
18. Harris MR. The problem of power factor in vrpm (transverse-flux) machines. In: Eighth international conference on electrical machines and drives, 1997;386–390. IEE, Cambridge, UK. https://doi.org/10.1049/cp:19971104.
19. Muller S, Keller M, Maier M, Parspour N. Comparison of iron loss calculation methods for soft magnetic composite. In: 2017 Brazilian power electronics conference (COBEP), 2017;1–6. IEEE, Juiz de Fora, Brazil . https://doi.org/10.1109/COBEP.2017.8257313.

20. Gartner M, Seibold P, Parspour N. Laminated circumferential transverse flux machines - lamination concept and applicability to electrical vehicles. In: 2011 IEEE international electric machines & drives conference (IEMDC), 2011;831–837. IEEE, Niagara Falls, Ontario, Canada. https://doi.org/10.1109/IEMDC.2011.5994921.
21. Pinguey E. On the design and construction of modulated pole machines. PhD thesis, Newcastle University 2010.
22. Schmid M, Terfurth J, Kaiser K, Parspour N. Electromagnetic design of electrical machines - new potentials of additive manufacturing with the example of the transverse flux machine. In: 2022 International Conference on Electrical Machines (ICEM), 2022;1491–1497. IEEE, Valencia, Spain. https://doi.org/10.1109/ICEM51905.2022.9910628.
23. Goll D, Schuller D, Martinek G, Kunert T, Schurr J, Sinz C, et al. Additive manufacturing of soft magnetic materials and components. Addit Manuf. 2019;27:428–39. https://doi.org/10.1016/j.addma.2019.02.021.
24. Kresse T, Schurr J, Lanz M, Kunert T, Schmid M, Parspour N, et al. Additively manufactured transverse flux machine components with integrated slits for loss reduction. Metals. 2022;12(11):1875. https://doi.org/10.3390/met12111875.
25. Knecht S, Schmid M, Reisch I, Parspour N, Albers A. Structural investigation of an additively manufactured stator of a transverse flux machine. In: Proceedings of the ASME 2024 international mechanical engineering congress and exposition. American Society of Mechanical Engineers, Portland, Oregon, USA 2024. https://doi.org/10.1115/IMECE2024-144893.
26. Zhang B. Modellierung und hocheffiziente berechnung der lastabhängigen eisenverluste in permanentmagneterregten synchronmaschinen. PhD thesis, Karlsruhe Institute of Technology 2019. https://doi.org/10.5445/KSP/1000093877.
27. Steinmetz CP. On the law of hysteresis. Trans Am Inst Electr Eng. 1892;9(1):1–64.
28. Bertotti G. General properties of power losses in soft ferromagnetic materials. IEEE Trans Magn. 1988;24(1):621–30. https://doi.org/10.1109/20.43994.
29. Guo Y, Zhu J, Lu H, Lin Z, Li Y. Core loss calculation for soft magnetic composite electrical machines. IEEE Trans Magn. 2012;48(11):3112–5. https://doi.org/10.1109/TMAG.2012.2197677.
30. Ballestín-Bernad V, Kulan MC, Baker NJ, Domínguez-Navarro JA. Power analysis in an smc-based aerospace transverse flux generator for different load and speed conditions. IEEE Trans Transp Electrif. 2025;11(2):5700–8. https://doi.org/10.1109/TTE.2024.3488899.
31. Zhang B, Wang AS, Doppelbauer M. Optimization of a transverse flux machine with claw-pole and flux-concentrating structure. In: 2015 IEEE international electric machines & drives conference (IEMDC), 2015;1735–1741. IEEE, Coeur d'Alene, Idaho, USA. https://doi.org/10.1109/IEMDC.2015.7409298.
32. Zhang C, Chen Z, Mei Q, Duan J. Application of particle swarm optimization combined with response surface methodology to transverse flux permanent magnet motor optimization. IEEE Trans Magn. 2017;53(12):1–7. https://doi.org/10.1109/TMAG.2017.2749565.
33. Hui J, Gao M, Wang Y. Design and optimisation of transverse flux machine with passive rotor and flux-concentrating structure. IET Electr Power Appl. 2019;13(7):922–31. https://doi.org/10.1049/iet-epa.2018.5793.
34. Zhang B, Wang A, Doppelbauer M. Multi-objective optimization of a transverse flux machine with claw-pole and flux-concentrating structure. IEEE Trans Magn. 2016;52(8):1–10. https://doi.org/10.1109/TMAG.2016.2554562.
35. Li Y, Jia H, Zhang A, Xiao B, Zhu Y, Wei T. Robust multi-objective transverse flux machine drive optimization considering torque ripple and manufacturing uncertainties. J Power Electr. 2023;23(6):935–44.
36. Jordan S, Baker NJ. Design and build of a mass critical, air-cooled transverse flux machine for aerospace. In: 2016 XXII international conference on electrical machines (ICEM), 1453–1458. IEEE, Lausanne, Switzerland 2016. https://doi.org/10.1109/ICELMACH.2016.7732715.
37. Yu B, Zhang S, Yan J, Cheng L, Zheng P. Thermal analysis of a novel cylindrical transverse-flux permanent-magnet linear machine. Energies. 2015;8(8):7874–96. https://doi.org/10.3390/en8087874.
38. Doering J, Steinborn G, Hofmann W, Dresden TU. Torque, power, losses and heat calculation of a transverse flux reluctance machine with soft magnetic composite materials and disc-shaped rotor. In: 2013 IEEE energy conversion congress and exposition, 2013;4326–4333. IEEE, Denver, Colorado, USA. https://doi.org/10.1109/ECCE.2013.6647279.
39. Hasan I, Husain T, Sozer Y, Husain I, Muljadi E. Mechanical and thermal performance of transverse flux machines. In: 2017 IEEE energy conversion congress and exposition (ECCE), 2017;1205–1211. IEEE, Cincinnati, Ohio, USA. https://doi.org/10.1109/ECCE.2017.8095926.
40. Yehorov A, Duniev O, Masliennikov A, Gouws R, Dobzhanskyi O, Stamann M. Study on the thermal state of a transverse-flux motor. IEEE Access. 2025;13:20893–902. https://doi.org/10.1109/ACCESS.2025.3534284.
41. Umland N, Winkler K, Inkermann D. Multidisciplinary design automation of electric motors–systematic literature review and methodological framework. Energies. 2023;16(20):7070.
42. Babcock T, McKeever B, Hicken JE. Multi-disciplinary design optimization of an electric motor considering thermal constraints. In: AIAA aviation 2023 Forum, 4342; 2023.
43. Xie B, Zhang Y, Xu Z, Zhang F. Rotor multidisciplinary optimization of high speed pmsm based on multi-fidelity surrogate model and gradient sequential sampling. IEEE Trans Energy Convers. 2022;38(2):859–68.
44. Lei G, Liu C, Guo Y, Zhu J. Multidisciplinary design analysis and optimization of a pm transverse flux machine with soft magnetic composite core. IEEE Trans Magn. 2015;51(11):1–4. https://doi.org/10.1109/TMAG.2015.2440429.
45. Pantelyat MG. Multiphysical numerical analysis of electromagnetic devices: State-of-the-art and generalization. Electr Eng Electromech. 2013;3:29–35. https://doi.org/10.20998/2074-272X.2013.3.06.
46. Keller M, Muller S, Parspour N. Design of a permanent magnetic excited transverse flux machine for robotic applications. In: 2016 XXII International conference on electrical machines (ICEM), 2016;1520–1525.
47. Hak J. Der luftspalt-wärmewiderstand einer elektrischen maschine. Electr Eng. 1956;42(5):257–72. https://doi.org/10.1007/BF01407415.
48. Eichler W, Tkotz K. Rechenbuch Elektrotechnik. Haan-Gruiten: Europa-Lehrmittel. Verl. Europa-Lehrmittel; 2020.
49. DIN: DIN EN 60085:2008-08: Electrical insulation - Thermal evaluation and designation (IEC 60085:2007); German version EN 60085:2008; 2008.

Publisher's Note